

Combined analysis of effective Higgs portal dark matter models

(arXiv: [1512.06458](https://arxiv.org/abs/1512.06458))

Ankit Beniwal¹, Filip Rajec¹, Christopher Savage, Pat Scott,
Christoph Weniger, Martin White¹, Anthony G. Williams¹

¹ARC Centre of Excellence for Particle Physics at the Terascale & CSSM,
Department of Physics, University of Adelaide, Adelaide, SA 5005, Australia

March 9, 2016



Australian Government
Australian Research Council



- Introduction
 - Dark Matter (DM)
 - Higgs portal
- Models
 - Scalar
 - Vector
 - Majorana fermion
 - Dirac fermion
- Constraints
 - Relic Density
 - Higgs Invisible width
 - Indirect Detection
 - Direct Detection
- Results
- Conclusions

Introduction

Dark Matter (DM)

- Non-luminous, non-interacting form of matter.
- Accounts for $\sim 27\%$ of the total matter-energy density in our Universe.
- Standard Model (SM) of Particle Physics does not provide “good” DM candidates.
- Forces us to look for candidates that lie Beyond the SM (BSM).
- Weakly Interacting Massive Particles (WIMPs) are popular DM candidates due to the *WIMP miracle*.

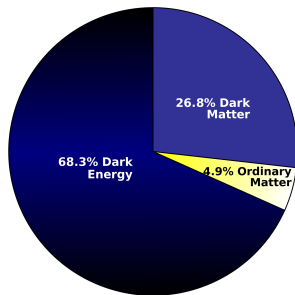


FIG. 1: Contributions to the total mass-energy density in our Universe [1].

- In the **bottom-up** Effective Field Theory (EFT) approach, one assumes a DM-SM interaction Lagrangian of the form

$$\mathcal{L}_{\text{int}} \supset \Lambda^{-n} \mathcal{O}_{\text{DM}} \mathcal{O}_{\text{SM}}, \quad (1)$$

where Λ is the EFT cut-off scale and \mathcal{O}_{DM} (\mathcal{O}_{SM}) are the DM (SM) operators, singlets under the SM gauge groups.

- In the **Higgs portal** scenario, $\mathcal{O}_{\text{SM}} = H^\dagger H$ where H is the SM Higgs doublet.
- Motivated by
 - The model simplicity in the required BSM particle content.
 - $H^\dagger H$ being one of the two lowest-dimensional gauge-invariant operators one can write in the SM.
- Recent discovery of the Higgs boson by the ATLAS [2] and CMS [3] experiments at the LHC gives us an extra experimental window.

- DM fields are assumed to be SM gauge singlets.
- Depending on the DM particle spin, the interaction potentials (\mathcal{V}) are

$$\text{Scalar} : \mathcal{V}_S = \frac{1}{2}\mu_S^2 S^2 + \frac{1}{4!}\lambda_S S^4 + \frac{1}{2}\lambda_{hS} S^2 H^\dagger H,$$

$$\text{Vector} : \mathcal{V}_V = -\frac{1}{2}\mu_V^2 V_\mu V^\mu + \frac{1}{4!}\lambda_V (V_\mu V^\mu)^2 - \frac{1}{2}\lambda_{hV} V_\mu V^\mu H^\dagger H,$$

$$\text{Majorana} : \mathcal{V}_\chi = \frac{1}{2}\mu_\chi \bar{\chi}\chi + \frac{1}{2}\frac{\lambda_{h\chi}}{\Lambda_\chi} \left(\cos\theta \bar{\chi}\chi + \sin\theta \bar{\chi}i\gamma_5\chi \right) H^\dagger H,$$

$$\text{Dirac} : \mathcal{V}_\psi = \mu_\psi \bar{\psi}\psi + \frac{\lambda_{h\psi}}{\Lambda_\psi} \left(\cos\theta \bar{\psi}\psi + \sin\theta \bar{\psi}i\gamma_5\psi \right) H^\dagger H,$$

where the parameter θ determines the type of interaction.

- To stabilise DM on cosmological time scales, impose an assumed \mathbb{Z}_2 symmetry: $X \rightarrow -X$ for $X \in (S, V_\mu, \chi, \psi)$.

- After the Electroweak Symmetry Breaking (EWSB)

$$H = \frac{1}{\sqrt{2}} \begin{pmatrix} 0 \\ v_0 + h \end{pmatrix}$$

where h is the physical SM Higgs field and $v_0 = 246.22$ GeV is the Higgs Vacuum Expectation Value (VEV).

- Consequently, the $H^\dagger H$ operator generates mass and interaction terms for the DM fields $X \in (S, V_\mu, \chi, \psi)$.

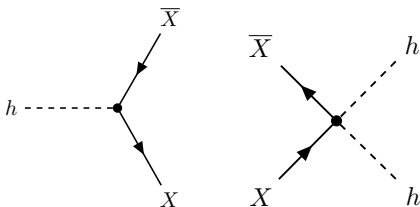


FIG. 2: Feynman diagrams for $h \rightarrow \bar{X}X$ and $\bar{X}X \rightarrow hh$.

- The scalar and vector model interaction potentials reduces to

$$\mathcal{V}_S = \frac{1}{2} m_S^2 S^2 + \frac{1}{4!} \lambda_S S^4 + \frac{1}{2} \lambda_S S^2 \left(v_0 h + \frac{1}{2} h^2 \right),$$

$$\mathcal{V}_V = -\frac{1}{2} m_V^2 V_\mu V^\mu + \frac{1}{4!} \lambda_V (V_\mu V^\mu)^2 - \frac{1}{2} \lambda_{hV} V_\mu V^\mu \left(v_0 h + \frac{1}{2} h^2 \right),$$

where the physical masses are

$$\text{Scalar : } m_S^2 = \mu_S^2 + \frac{1}{2} \lambda_{hS} v_0^2, \quad \text{Vector : } m_V^2 = \mu_V^2 + \frac{1}{2} \lambda_{hV} v_0^2.$$

- When $\sin \theta \neq 0$ in fermion models, non mass-type contributions appear. We redefine the fields through chiral rotation

$$\text{Majorana} : \chi \rightarrow \exp(i\gamma_5\alpha/2)\chi, \quad \text{Dirac} : \psi \rightarrow \exp(i\gamma_5\alpha/2)\psi,$$

where α is a real, space-time independent parameter.

- Ultimately, the Majorana and Dirac fermion model interaction potentials reduces to

$$\text{Majorana} : \mathcal{V}_\chi = \frac{1}{2} m_\chi \bar{\chi}\chi + \frac{1}{2} \frac{\lambda_{h\chi}}{\Lambda_\chi} \left(\cos \xi \bar{\chi}\chi + \sin \xi \bar{\chi} i \gamma_5 \chi \right) \left(v_0 h + \frac{1}{2} h^2 \right),$$

$$\text{Dirac} : \mathcal{V}_\psi = m_\psi \bar{\psi}\psi + \frac{\lambda_{h\psi}}{\Lambda_\psi} \left(\cos \xi \bar{\psi}\psi + \sin \xi \bar{\psi} i \gamma_5 \psi \right) \left(v_0 h + \frac{1}{2} h^2 \right),$$

where $\xi \equiv \theta + \alpha$ and the physical masses are

$$m_{\chi,\psi} = \sqrt{\left(\mu_{\chi,\psi} + \frac{1}{2} \frac{\lambda_{h\chi,h\psi}}{\Lambda_{\chi,\psi}} v_0^2 \cos \theta \right)^2 + \left(\frac{1}{2} \frac{\lambda_{h\chi,h\psi}}{\Lambda_{\chi,\psi}} v_0^2 \sin \theta \right)^2}.$$

Free model parameters

- Scalar: m_S, λ_{hS}
- Vector: m_V, λ_{hV}
- Majorana fermion: $m_\chi, \lambda_{h\chi}/\Lambda_\chi, \cos \xi$
- Dirac fermion: $m_\psi, \lambda_{h\psi}/\Lambda_\psi, \cos \xi$

In fermion models, consider

- $\cos \xi = 1 \implies$ *pure scalar* interaction,
- $\cos \xi = 1/\sqrt{2} \implies$ *equally mixed scalar-pseudoscalar* interaction,
- $\cos \xi = 0 \implies$ *pure pseudoscalar* interaction.

Model parameters are constrained using

- Relic Density,
- Higgs Invisible width,
- Indirect Detection,
- Direct Detection.

Relic Density

- Mass density of DM particles at the time of 'freeze-out'.
- The best known value comes from the Planck satellite [1]

$$\Omega_{\text{DM}} h^2 = 0.1199 \pm 0.0027, \quad (2)$$

where $\Omega_{\text{DM}} \equiv \rho_{\text{DM}}/\rho_c$, $\rho_c = 3H_0^2/8\pi G$ is the critical mass density and $h = H_0/(100 \text{ km s}^{-1} \text{ Mpc}^{-1})$ is the reduced Hubble constant.

- For WIMPs annihilating purely via the s -channel,

$$\Omega_{\text{DM}} h^2 \sim \frac{3 \times 10^{-27} \text{ cm}^3 \text{ s}^{-1}}{\langle \sigma v_{\text{rel}} \rangle}$$

where $\langle \sigma v_{\text{rel}} \rangle$ is the velocity-averaged annihilation cross-section.

- At fixed DM masses, Eq. (2) restricts the allowed value(s) of the Higgs-DM coupling.
- Define a relic abundance parameter $f_{\text{rel}} \equiv \Omega_X/\Omega_{\text{DM}}$ where $X \in (S, V, \chi, \psi)$ and consider $f_{\text{rel}} = 1$ (100%), 0.1 (10%) and 0.01 (1%).

Higgs Invisible width

- When $m_X < m_h/2$, the decay $h \rightarrow \bar{X}X$ for $X \in (S, V, \chi, \psi)$ is kinematically allowed and contributes to the invisible width $\Gamma_{\text{inv}}(h \rightarrow \bar{X}X)$ of the SM Higgs boson.
- On the SM Higgs invisible branching ratio

$$\mathcal{BR}(h \rightarrow \bar{X}X) = \frac{\Gamma_{\text{inv}}}{\Gamma_{\text{inv}} + \Gamma_{\text{SM}}}, \quad (3)$$

an upper limit of 19% at 2σ CL [4] and a projected limit of 5% at 1σ CL [5] is placed.

- Using the upper limits on Eq. (3) and Γ_{inv} expressions in our models, upper limits on the Higgs-DM coupling is placed as a function of the DM mass up to $m_h/2$.

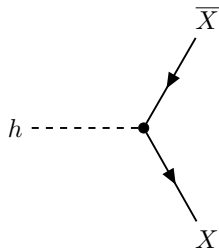


FIG. 3: Invisible decay of the Higgs boson into $\bar{X}X$ where $X \in (S, V, \chi, \psi)$.

Indirect Detection

- Searches for fluxes of γ -rays, e^\pm , p^\pm and neutrinos produced from DM annihilations.
- The annihilation flux $\Phi_{\text{ann}} \propto \rho_{\text{DM}}^2$ where ρ_{DM} is the DM mass density.
- Natural targets include dwarf spheroidal (dSph) galaxies, the Galactic Centre (GC) or our Sun.
- Experiments include the Fermi Large Area Telescope (Fermi-LAT), H.E.S.S, AMS-02 and the upcoming Cherenkov Telescope Array (CTA).

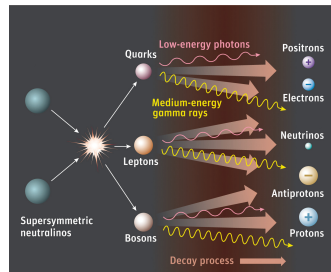


FIG. 4: Indirect detection of DM.

- To impose indirect search limits, use a combined log-likelihood function

$$\ln \mathcal{L}_{\text{total}} = \ln \mathcal{L}_{\text{CMB}} + \ln \mathcal{L}_{\text{dSphs}} + \ln \mathcal{L}_{\text{CTA}},$$

which depends on the model parameters.

- **Current** limits are derived using
 - 7-years observation of the Cosmic Microwave Background (CMB) by WMAP,
 - Combined analysis of 15 dwarf spheroidals (dSphs) satellite galaxies using 6-years of the Fermi-LAT data.
- Projected **future** limits are generated using
 - Polarization of the CMB as measured by the Planck satellite,
 - Projected improvements in the Fermi-LAT sensitivity towards observing additional dwarf spheroidals (dSphs),
 - Projected sensitivities of the upcoming Cherenkov Telescope Array (CTA).
- Scale all indirect search signals by $f_{\text{rel}}^2 = (\Omega_X / \Omega_{\text{DM}})^2$ where $X \in (S, V, \chi, \psi)$.
- Weak indirect search limits exist in fermion models when $\cos \xi = 1$ due to a velocity-suppressed annihilation cross-section $\langle \sigma v_{\text{rel}} \rangle$.

CMB Likelihood

- Temperature fluctuations and polarization of the CMB is sensitive to the redshift of recombination $z \sim 1100$, since it determines the surface of last scattering.
- If DM annihilates or decays after $z \sim 1100$, the deposited EM radiation can delay the time taken for recombination and/or produce distortions in the CMB.
- We use the WMAP and Planck log-likelihood functions from Ref. [6], which depends on the effective efficiency f_{eff} of producing ionisation radiation from DM annihilations, and on the model parameters.

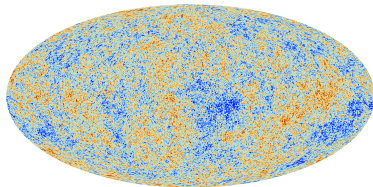


FIG. 5: CMB anisotropies as measured by the Planck satellite.

Fermi dwarfs Likelihood

- Powerful tool in searching for signs of DM annihilations in distant astrophysical sources.
- Provides the strongest upper limits on $\langle\sigma v_{\text{rel}}\rangle$ from a combined analysis of 15 dSphs using 6-years of the Fermi-LAT data [7].
- Results available in the form of tabulated energy times integrated gamma-ray flux ($E\Phi_{\text{ann}}$) and log-likelihoods ($\ln \mathcal{L}$) values.
- For the projected Fermi-LAT limits, scale the current limits by $\sqrt{2 \times 10/6} \sim 1.83$.



FIG. 6: The Fermi-LAT space telescope.

CTA Likelihood

- Multi-national project to build the next generation of ground-based gamma-ray instruments.
- Sensitivity to energies from a few tens of GeV to 100 TeV and flux by an order of magnitude from the current Imaging Atmospheric Cherenkov Telescopes (IACTs) such as MAGIC [8], H.E.S.S. [9] and VERITAS [10].
- Several tens of telescopes of 2-3 different types, with size varying between 5 and 25 metres, distributed over an area of several square kilometres.
- Envisaged as a two part telescope with southern and northern sites. CTA South is most relevant for DM searches towards the GC.

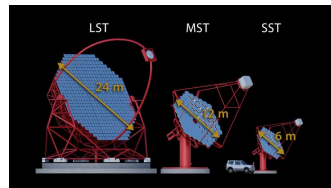


FIG. 7: Planned types of telescopes for the CTA.



FIG. 8: A prototype of the Large-sized Telescope (LST).

- Use the tabulated energy integrated gamma-ray flux $E\Phi_{\text{ann}}$ and log-likelihood values from Ref. [11] based on
 - A morphological analysis over the relevant Regions of Interest (RoI).
 - Assuming $\gtrsim 100$ hrs of GC observation by CTA,
 - 1% instrumental systematic uncertainty,
 - Inclusion of all known backgrounds (cosmic ray electrons/protons and the galactic diffuse emissions (GDE)),
 - J -factors (line-of-sight and solid angle integral of the squared DM density) for the GC using the Einasto profile

$$\rho_{\text{DM}}(r) \propto \exp\left(-\frac{2}{\alpha} \left[\left(\frac{r}{r_s}\right)^\alpha - 1\right]\right), \quad (4)$$

where the local DM density $\rho_{\text{DM}}(r_\odot) = 0.4 \text{ GeV cm}^{-3}$ by choosing $\alpha = 0.17$, $r_s = 20 \text{ kpc}$ and $r_\odot = 8.5 \text{ kpc}$ [12].

- Use a contracted generalised NFW profile

$$\rho_{\text{DM}}(r) \propto \frac{1}{r^\gamma (r_s + r)^{3-\gamma}}, \quad \gamma = 1.3,$$

which leads to a factor of 6 better limits on $\langle\sigma v_{\text{rel}}\rangle$ [11].

Direct Detection

- Experiments aim to measure the recoil of a nucleus in a collision with a DM particle.
- Currently, the strongest upper limits on the Spin-Independent (SI) WIMP-nucleon cross-section σ_{SI} comes from the LUX experiment [13].
- Using expressions for σ_{SI} in our models, direct search limits from the LUX (current limits) and projected XENON1T (future limits) experiments are imposed.
- Scale direct search limits by $f_{\text{rel}} = \Omega_X / \Omega_{\text{DM}}$ where $X \in (S, V, \chi, \psi)$.
- In fermion models when $\cos \xi = 0$, the SI cross-section is momentum-suppressed by a factor of $q^2/4m_{\chi, \psi}^2$, leading to weak direct search limits.

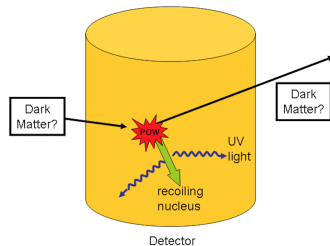


FIG. 9: DM-nucleus interaction in a typical DM search experiment.

Results

Scalar model: Relic density contours

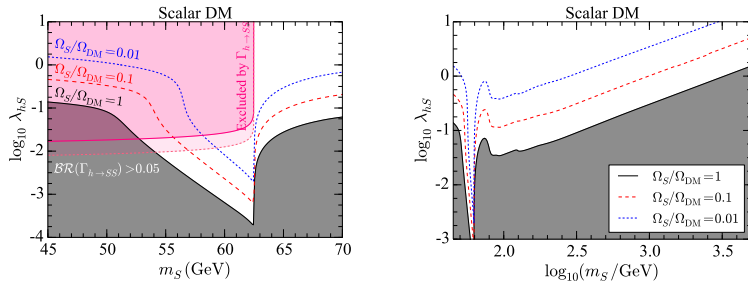


FIG. 10: Scalar relic density contours in the low mass (*left*) and high mass (*right*) range for $f_{\text{rel}} = 1$ (black solid), 0.1 (red dashed) and 0.01 (blue dotted). Grey and pink shaded regions are excluded respectively by the relic density and the Higgs invisible width constraints.

Results

Scalar model: Indirect search limits

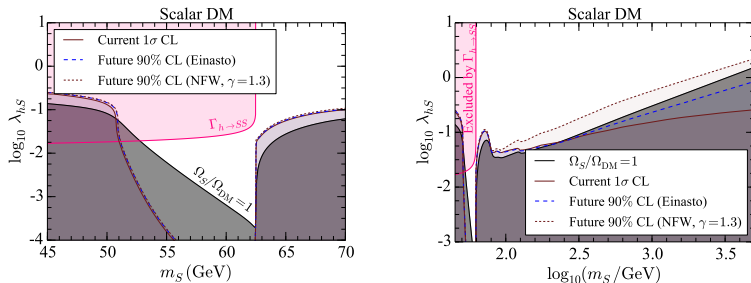


FIG. 11: Indirect search limits in the low mass (*left*) and high mass (*right*) range. Grey and pink shaded regions are excluded respectively by the relic density and an upper limit of 19% on $\mathcal{BR}(h \rightarrow SS)$ at 2σ CL. Values of λ_{hS} below the current 1σ CL (brown solid) curve are excluded at more than 1σ CL. Regions below the future 90% CL curve with the Einasto (blue dashed) and contracted NFW (brown dotted) profile will be excluded.

Results

Scalar model: Direct search limits

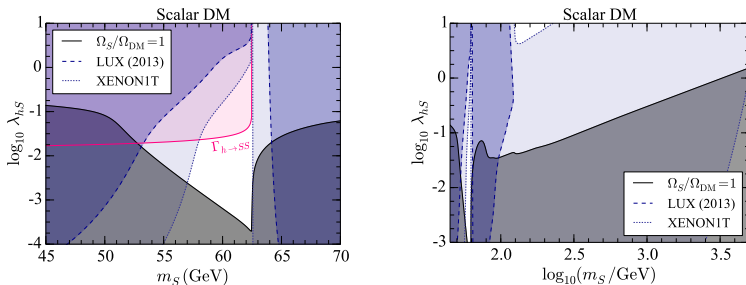


FIG. 12: Direct search limits in the low mass (*left*) and high mass (*right*) range. Grey and pink shaded regions are excluded respectively by the relic density and an upper limit of 19% on $\mathcal{BR}(h \rightarrow SS)$ at 2σ CL. Regions excluded by the LUX (XENON1T) experiment are delineated with blue dashed (blue dotted) curves and dark (light) shadings.

Results

Vector model: Relic density contours

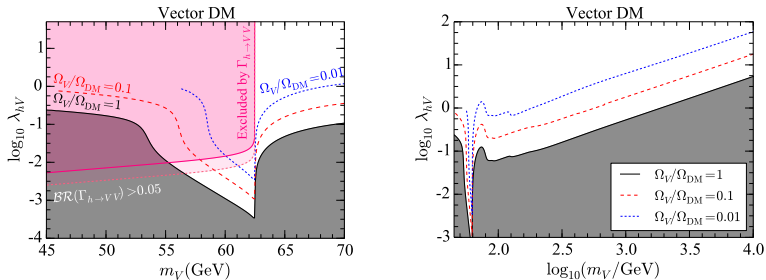


FIG. 13: Vector relic density contours in the low mass (*left*) and high mass (*right*) range for $f_{\text{rel}} = 1$ (black solid), 0.1 (red dashed) and 0.01 (blue dotted). Grey and pink shaded regions are excluded respectively by the relic density and the Higgs invisible width constraints.

Results

Vector model: Indirect search limits

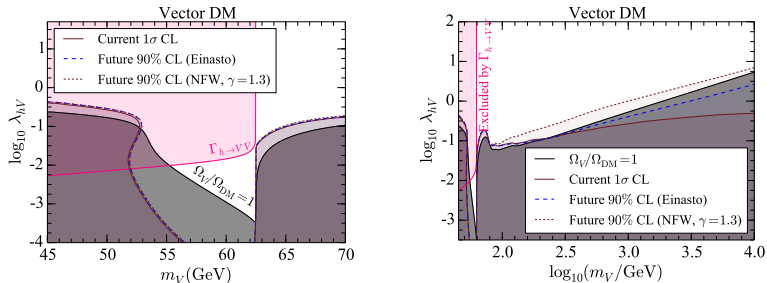


FIG. 14: Indirect search limits in the low mass (*left*) and high mass (*right*) range. Grey and pink shaded regions are excluded respectively by the relic density and an upper limit of 19% on $\mathcal{BR}(h \rightarrow VV)$ at 2 σ CL. Values of λ_{hV} below the current 1 σ CL (brown solid) curve are excluded at more than 1 σ CL. Regions below the future 90% CL curve with the Einasto (blue dashed) and contracted NFW (brown dotted) profile will be excluded.

Results

Vector model: Direct search limits

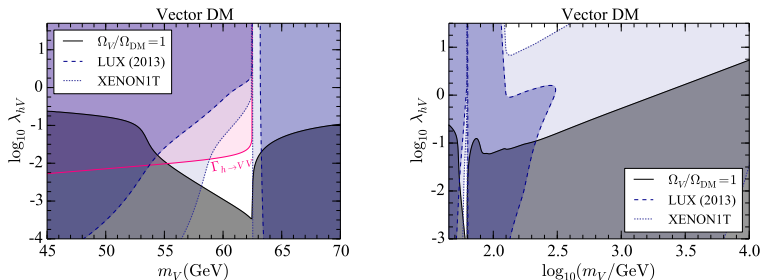


FIG. 15: Direct search limits in the low mass (*left*) and high mass (*right*) range. Grey and pink shaded regions are excluded respectively by the relic density and an upper limit of 19% on $\mathcal{BR}(h \rightarrow VV)$ at 2σ CL. Regions excluded by the LUX (XENON1T) experiment are delineated with blue dashed (blue dotted) curves and dark (light) shadings.

Results

Majorana fermion model: Relic density contours

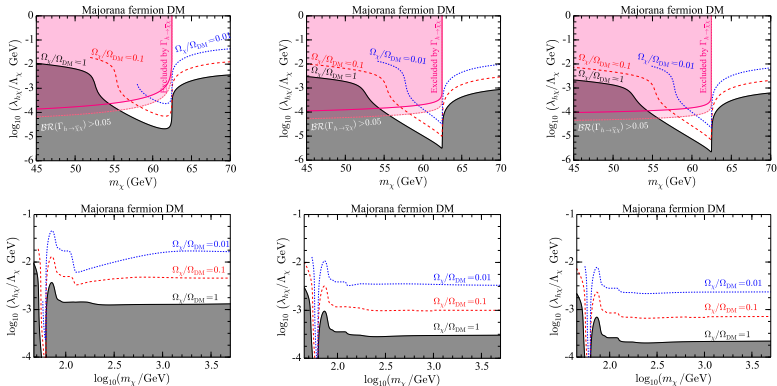


FIG. 16: Majorana fermion relic density contours in the low mass (*top row*) and high mass (*bottom row*) range for $f_{\text{rel}} = 1$ (black solid), 0.1 (red dashed) and 0.01 (blue dotted) with $\cos \xi = 1$ (*left*), $1/\sqrt{2}$ (*center*) and 0 (*right*). Grey and pink shaded regions are excluded respectively by the relic density and the Higgs invisible width constraints.

Results

Majorana fermion model: Indirect search limits

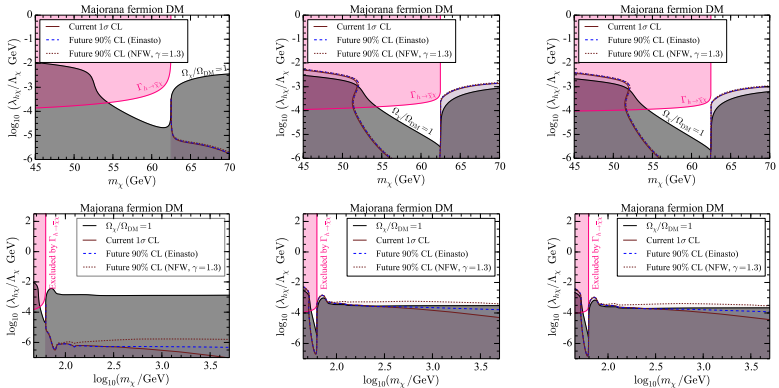


FIG. 17: Indirect search limits in the low mass (*top row*) and high mass (*bottom row*) range with $\cos \xi = 1$ (*left*), $1/\sqrt{2}$ (*center*) and 0 (*right*). Grey and pink shaded regions are excluded respectively by the relic density and an upper limit of 19% on $\mathcal{BR}(h \rightarrow \bar{\chi}\chi)$ at 2σ CL. Values of $\lambda_{h\chi}/\Lambda_\chi$ below the current 1σ CL (brown solid) curve are excluded at more than 1σ CL. Regions below the future 90% CL curve with the Einasto (blue dashed) and contracted NFW (brown dotted) profile will be excluded.

Results

Majorana fermion model: Direct search limits

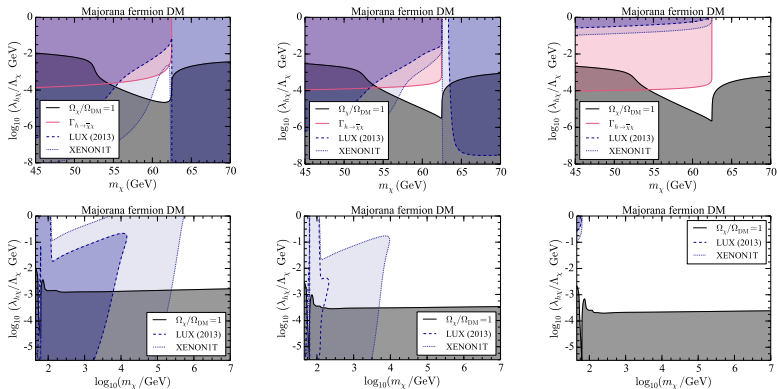


FIG. 18: Direct search limits in the low mass (*top row*) and high mass (*bottom row*) range with $\cos \xi = 1$ (*left*), $1/\sqrt{2}$ (*center*) and 0 (*right*). Grey and pink shaded regions are excluded respectively by the relic density and an upper limit of 19% on $\mathcal{BR}(h \rightarrow \bar{\chi}\chi)$ at 2σ CL. Regions excluded by the LUX (XENON1T) experiment are delineated with blue dashed (blue dotted) curves and dark (light) shadings.

Results

Dirac fermion model: Relic density contours

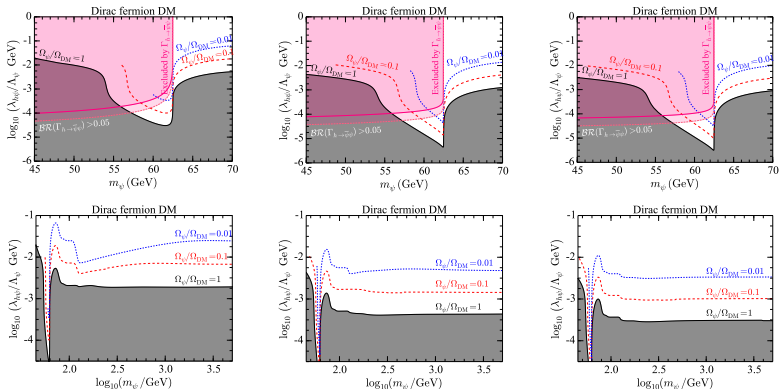


FIG. 19: Dirac fermion relic density contours in the low mass (*top row*) and high mass (*bottom row*) range for $f_{\text{rel}} = 1$ (black solid), 0.1 (red dashed) and 0.01 (blue dotted) with $\cos \xi = 1$ (*left*), $1/\sqrt{2}$ (*center*) and 0 (*right*). Grey and pink shaded regions are excluded respectively by the relic density and the Higgs invisible width constraints.

Results

Dirac fermion model: Indirect search limits

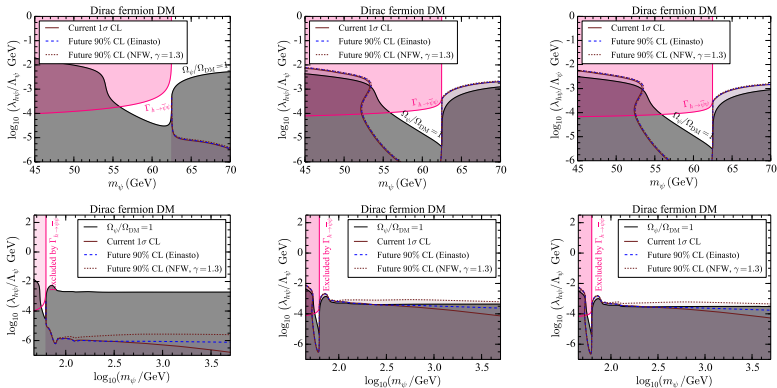


FIG. 20: Indirect search limits in the low mass (*top row*) and high mass (*bottom row*) range with $\cos \xi = 1$ (*left*), $1/\sqrt{2}$ (*center*) and 0 (*right*). Grey and pink shaded regions are excluded respectively by the relic density and an upper limit of 19% on $\mathcal{BR}(h \rightarrow \bar{\psi}\psi)$ at 2σ CL. Values of $\lambda_{h\psi}/\Lambda_\psi$ below the current 1σ CL (brown solid) curve are excluded at more than 1σ CL. Regions below the future 90% CL curve with the Einasto (blue dashed) and contracted NFW (brown dotted) profile will be excluded.

Results

Dirac fermion model: Direct search limits

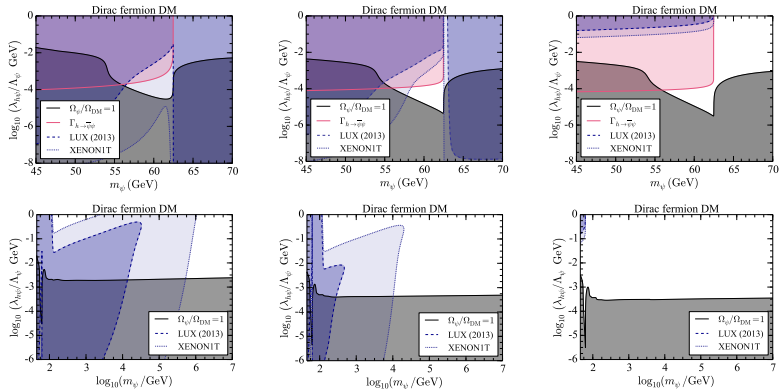


FIG. 21: Direct search limits in the low mass (*top row*) and high mass (*bottom row*) range with $\cos \xi = 1$ (*left*), $1/\sqrt{2}$ (*center*) and 0 (*right*). Grey and pink shaded regions are excluded respectively by the relic density and an upper limit of 19% on $\mathcal{BR}(h \rightarrow \bar{\psi}\psi)$ at 2σ CL. Regions excluded by the LUX (XENON1T) experiment are delineated with blue dashed (blue dotted) curves and dark (light) shadings.

Conclusions

- A combined analysis of all four effective Higgs portal DM models. In fermion models, an admixture of scalar-pseudoscalar interaction terms is taken.
- A consistent study of indirect search prospects from the current and future based gamma-ray experiments.
- Included the $q^2/4m_{\chi,\psi}^2$ factor in the SI cross-section to correctly compute the direct search event rates in fermion models when $\cos \xi = 0$ (pure pseudoscalar interaction).
- Combined constraints on the DM relic density and the Higgs invisible width rule out most of the low mass parameter space, apart from a small triangular region near $m_h/2$. Entire resonance region in the Dirac fermion model when $\cos \xi = 1$ will be excluded by the projected XENON1T experiment.
- Indirect search limits are weak when compared against the combined DM relic density, Higgs invisible width and direct search constraints. However, they are our *only* hope in accessing the high fermion DM mass range when $\cos \xi = 0$. The upcoming CTA experiment will be useful in this regard.
- Direct search experiments will continue to provide the strongest limits on the parameter space of all models.

Thanks for your attention!

- [1] **Planck Collaboration**, P. Ade et al., *Planck 2013 results. XVI. Cosmological parameters*, *Astron.Astrophys.* **571** (2014) A16, [[arXiv:1303.5076](#)].
- [2] **ATLAS Collaboration**, G. Aad et al., *Observation of a new particle in the search for the Standard Model Higgs boson with the ATLAS detector at the LHC*, *Phys. Lett.* **B716** (2012) 1–29, [[arXiv:1207.7214](#)].
- [3] **CMS Collaboration**, S. Chatrchyan et al., *Observation of a new boson at a mass of 125 GeV with the CMS experiment at the LHC*, *Phys. Lett.* **B716** (2012) 30–61, [[arXiv:1207.7235](#)].
- [4] G. Belanger, B. Dumont, U. Ellwanger, J. Gunion, and S. Kraml, *Global fit to Higgs signal strengths and couplings and implications for extended Higgs sectors*, *Phys. Rev.* **D88** (2013) 075008, [[arXiv:1306.2941](#)].
- [5] M. E. Peskin, *Comparison of LHC and ILC Capabilities for Higgs Boson Coupling Measurements*, [arXiv:1207.2516](#).
- [6] J. M. Cline and P. Scott, *Dark Matter CMB Constraints and Likelihoods for Poor Particle Physicists*, *JCAP* **1303** (2013) 044, [[arXiv:1301.5908](#)].
- [7] **Fermi-LAT**, M. Ackermann et al., *Searching for Dark Matter Annihilation from Milky Way Dwarf Spheroidal Galaxies with Six Years of Fermi Large Area Telescope Data*, *Phys. Rev. Lett.* **115** (2015), no. 23 231301, [[arXiv:1503.02641](#)].
- [8] J. Aleksić et al., *Performance of the MAGIC stereo system obtained with Crab Nebula data*, *AstroPhys.* **35** (2012) 435–448, [[arXiv:1108.1477](#)].
- [9] **HESS Collaboration**, F. Aharonian et al., *Observations of the Crab Nebula with H.E.S.S.*, *Astron. Astrophys.* **457** (2006) 899–915, [[astro-ph/0607333](#)].
- [10] J. Holder et al., *Status of the VERITAS Observatory*, *AIP Conf. Proc.* **1085** (2009) 657–660, [[arXiv:0810.0474](#)].
- [11] H. Silverwood, C. Weniger, P. Scott, and G. Bertone, *A realistic assessment of the CTA sensitivity to dark matter annihilation*, *JCAP* **1503** (2015), no. 03 055, [[arXiv:1408.4131](#)].
- [12] L. Pieri, J. Lavalle, G. Bertone, and E. Branchini, *Implications of high-resolution simulations on indirect dark matter searches*, *Phys. Rev. D* **83** (2011), no. 2 023518, [[arXiv:0908.0195](#)].
- [13] **LUX**, D. S. Akerib et al., *First results from the LUX dark matter experiment at the Sanford Underground Research Facility*, *Phys. Rev. Lett.* **112** (2014) 091303, [[arXiv:1310.8214](#)].